Energetic Au ion beam implantation of ZnO nanopillars for optical response modulation

A. Macková*[ab], P. Malinský[ab], A. Jagerova[ab], R. Mikšová[a], O. Lalik[ab], P. Nekvindová[c], Z. Sofer[c], P. Marvan[c], V. Holý[de], J. D. Schutter[f], U. Kentsch[g], A. Azarov[h], A. Galeckas[h]

[a] *Nuclear Physics Institute of the Czech Academy of Sciences, v. v. i., 250 68 Řež, Czech Republic*

[b] *Department of Physics, Faculty of Science, J. E. Purkinje University, Pasteurova 3544/1, 400 96 Ústí nad Labem, Czech Republic*

[c] *Department of Inorganic Chemistry, University of Chemistry and Technology, 166 28 Prague, Czech Republic*

[d] *Department of Condensed Matter, Faculty of Mathematics and Physics, Charles University, Ke Karlovu 2026/5, 121 16 Prague 2, Czech Republic*

[e] *Faculty of Science, Masaryk University, Kotlářská 2, 61137 Brno, Czech Republic*

[f] *Budesanstalt für Materialforschung and Prüfung, Unter den Eichen 87, 12205, Berlin, Germany*

[g] *Helmholtz-Zentrum Dresden-Rossendorf, Institute of Ion Beam Physics and Materials Research, Bautzner Landstraße 400, 01328, Dresden, Germany*

[h] *Department of Physics, Centre for Material Science and Nanotechnology, University of Oslo, P.O. Box 1048, Blindern, N-0316 Oslo, Norway*

**corresponding author: mackova@ujf.cas.cz*

Abstract

Nanopillars of ZnO were implanted with Au-400keV ions at various ion fluences from 1×10^{15} cm^{-2} to 1×10^{16} cm^{-2} and subsequently annealed at 750 °C for 15 minutes in order to reduce the implantation damage and to support Au nanoparticle aggregation. It was found that implantation-induced effects and thermal effects influence the Au nanoparticle coalescence as well as the quality of the ZnO nanopillars. The implantation at the higher fluences induced the sharpening of the nanopillar upper parts and the compaction of the nanopillar bases, which are turned into a continuous layer after annealing**.** Luminescence measurement showed the surface plasmon resonance activity of the Au nanoparticles. The absorption maximum is evidenced from 500–650 nm and it is ascribed to Au nanoparticles or more complex Au-clusters. We observe the more pronounced intensity of the absorption peak (SPR) ascribed to the Au nanoparticles with the increased Au-ion fluence and after the annealing.

Keywords

ZnO nanopillars; Au nanoparticles, ion implantation; SPR; doped ZnO nanostructures

1. Introduction

We present our recent results obtained in Au-ion implantation of ZnO nanopillars for Au nanoparticle creation. Ion implantation is a versatile technique that makes it possible, by adjusting the implantation ion energy and fluence, to modify the electrical, mechanical and optical properties of bulk and nanostructured materials [1,2], as well as to introduce micro- and nano-structures via energetic heavy

ions. ZnO reportedly has an extraordinarily high radiation tolerance in comparison to other semiconducting materials such as GaN or GaAs [3]. However, due to ZnO's wide band gap energy of 3.37 eV at room temperature, large free exciton energy (60 meV) and high luminescence efficiency [4, 5], nanostructuring in ZnO has become very attractive and challenging for the preparation of nano-optics devices, as well as for DNA sensor and biological applications in general [6-8]. Au-metal nanoparticles can expand the light absorption range of ZnO and can greatly enhance the ZnO photocatalytic activity given their plasmonic or luminescence properties. Metal oxides such as ZnO are nowadays being investigated as efficient photocatalysts and antimicrobials agents [9]. The optical activity of metal nanoparticles (NPs) is strongly affected by their shape, size, geometrical configuration, structure and composition. Ion implantation and irradiation are unique tools for the synthesis and modification of nanoparticles in various host matrices and semiconductors as well. Since implanted noble metal-ions have larger radii than Zn, they tend to coalesce while inducing a dense collision cascade, which strongly modifies the ZnO wurtzite host matrix [10,11]. Semiconductor nanocrystallites with a dopant can exhibit unique optical and electronic properties [12,13], mainly in the case of Au [14]. However, the basis for the future research would be the published works devoted to the formation of radiation defects in ZnO (mainly *c*-plane-oriented), where significant connections between the dopant's chemical nature and defect formation have been investigated [3,10,11,15,16]. Damage accumulation, dopant positioning and defect–dopant interaction influencing defect stabilisation in bulk ZnO etc., are all crucial issues for the understanding of the complex processes taking place in ion beam irradiated ZnO nanopillars.

Nowadays, ZnO thin films and nanostructures can be synthesised by using various deposition techniques, such as molecular beam epitaxy (MBE) [17], metal–organic chemical vapour deposition (MOCVD) [18], chemical vapour deposition (CVD) [19] etc. ZnO possesses a large variety of nanostructures whose optical properties have been very intensively investigated [20]. Owing to its highly anisotropic wurtzite structure, vertically aligned ZnO nanowires can be formed as building blocks in a wide variety of applications [21,22].

Post-implantation annealing is typically used to restore the crystalline structure and also to improve the optical properties [23]. It should be noted that the removal of point defects is already observed at temperatures below 500 °C in single crystalline ZnO due to strong annealing of uncorrelated defect structures such as point defects and small defect clusters [24]. A complete removal of ion-induced extended defects in single crystalline ZnO typically requires relatively high temperatures exceeding 900–1000 °C, as reported for other ion species including Ag in [25,26]. Furthermore, the implanted atoms themselves can stabilise radiation defects, while pronounced loss or out-diffusion of implanted atoms may lead to efficient recovery of the crystalline lattice and coalescence of the introduced dopant.

The situation differs in ZnO nanostructures, where radiation defects in the Ag-implanted nanorods can be successfully recovered using RTA (Rapid Thermal Annealing) in oxygen at lower temperatures between 700 °C and 950 °C. Sufficient annealing has to be performed in order to remove the implantation defects; short duration and low enough temperature annealing is desirable in order not to degrade the implanted ZnO nanorods [28]. Moreover, moderate annealing is necessary to avoid deactivating the dopants [28]. It was observed in [27] that temperatures from 700 °C to 900 °C for 15 minutes can recover the outer shell of the ZnO nanowire from 35 to 70 nm thick, respectively. However, at the higher temperature, the nanowire exhibits rough side facets instead of the perfectly flat ones for as-grown samples. The surface degradation has been ascribed to annealing-induced

surface degradation of the implanted ZnO nanowires in [27] and a thermal deterioration effect was confirmed also in high As-ion fluence implanted nanorods after annealing at 950–1000 °C in [29].
It was demonstrated that the dislocation elimination in ZnO nanowires is facilitated by the nanowire free surfaces, allowing shorter duration annealing at lower temperatures [29], and increasing the time of annealing above 20 minutes can be detrimental rather than beneficial. Au nanoparticle coalescence in materials such as sapphire after Au implantation can be achieved already at temperatures of about 600 °C [30], but typically longer annealing times are chosen to cause the coalescence of particles bigger than 10 nm. The photoluminescence (PL) of nanowires has been nearly fully recovered after annealing at 800 °C, with 15 min under vacuum in [31]. Optical properties can be tuned in various crystallographic orientations of ZnO by a distinct method [32]. The photoluminescence (PL) spectra have revealed that the near band gap (NBE) exciton-related luminescence band of Au:ZnO samples was partially restored for all crystal planes after thermal annealing at 600 °C due to the recovery of the ZnO structure. After the annealing, the NBE band was restored with the highest intensity in the *c*-plane [32].
Our experiments were motivated by the following issues: i) the structural damage in ZnO nanopillars after the Au-ion implantation and its recovery after the annealing, ii) Au incorporation and nanoparticle formation in ZnO nanopillars, iii) optical and luminescence properties of ion beam modified ZnO nanopillars.

2. Experiment

2.1. ZnO nanopillars growth and 400 keV Au^+ ion implantation

ZnO nanopillars were grown on Si wafers using a hydrothermal approach [33]. Polished silicon wafers 1 x 1 cm in size from Siegert Wafer (Germany) with the orientation of <100> ± 5° were immersed for 10 min in a 75 °C solution of deionised H_2O (0.055 μS/cm, Evoqua, USA), NH_3 (30%, Chemsolute, Germany), H_2O_2 (25%, Chemsolute, Germany) in the ratios of 5:1:1, followed by rinsing in deionised H_2O and a further cleaning two times in an ultrasonic bath. Afterwards, they were dipped for 20 s in a solution of 0.005 mol/l zinc acetate (Alfa Aesar, UK) in isopropanol (Chemsolute, Germany) and rinsed immediately with isopropanol. This procedure was repeated four times to assure a continuous coverage of zinc acetate. The samples were heated for 20 min at 350 °C to get a thin layer of calcined ZnO seeds on the silicon substrate. The samples were placed almost vertically in 50 ml centrifuge tubes, with the top side facing slightly downwards. An equimolar solution of 0.05 mol/l zinc nitrate (Alfa Aesar, UK) and hexamethylenetetramine (Alfa Aesar, UK) in deionised H_2O was used as deposition solution. The closed tubes were heated to 85 °C for 1 h. Finally, the samples were cleaned five times in an ultrasonic bath with deionised H_2O. ZnO nanopillars were implanted with the Au-400 keV ions using the fluences of 1×10^{15} cm^{-2}, 5×10^{15} cm^{-2} and 1×10^{16} cm^{-2} using an implantor at the Ion Beam Center, HZDR Dresden-Rossendorf, Germany. The implanted samples were subsequently annealed at ambient atmosphere at 750 °C for 15 minutes in a conventional furnace in order to reduce the implantation damage and to support Au nanoparticle aggregation.

2.2. Structure analysis of ZnO nanopillars with implanted Au by XRD, RBS and SEM

We used a Rigaku SMARTLAB 9 kW rotating-anode generator and Cu$K\alpha_1$ characteristic radiation; the diffractometer was equipped with a primary parabolic multi-layered mirror and a 2x220 Ge channel-cut monochromator. X-ray diffraction (XRD) was utilised for the study of the crystal-structure modification of the pristine ZnO nanopillars as well as those with Au nanoparticles. In the case of nanopillars, the MR setup was used, and we measured long-range 2Θ-scans keeping the incidence

angle constant ($\alpha_i = 0.4$ deg). High-resolution (HR) almost symmetric $2\Theta/\omega$ scans were measured using a secondary 2x220 Ge channel-cut analyser crystal; in these scans we avoided very intense diffraction peaks of Si substrate by introducing the angular offset of $\theta - \omega = 5$ deg.
Rutherford Back-Scattering spectrometry (RBS) was employed for characterisation of ZnO nanopillars using a beam of 2.0 MeV He^+ ions from a Tandetron accelerator using the detector placed at scattering angle 170°. Simultaneously, RBS was used for the implanted Au depth profile analysis.

Scanning electron microscopy (SEM) was realised using a TESCAN MAIA 3 instrument with a field emission gun (TESCAN, Czech Republic). All samples were attached to SEM stubs using double-sided conductive carbon tape. For side-view imaging, a small piece of Si substrate was cleaved to expose the transition between the substrate and ZnO nanopillars. For all samples, imaging was performed in high vacuum at 5 kV accelerating voltage using an in-beam detector.

2.3. Optical properties of ZnO nanopillars implanted with Au optical ellipsometry, PL spectroscopy

ZnO nanopillars were investigated by PL measurements carried out at 10K by employing a closed-cycle He refrigerator system and using a 325 nm wavelength He-Cd laser as an excitation source (power density ~20W/cm^2). The PL spectra were recorded by fibre optic spectrometers (Ocean Optics HR4000/USB4000).

The spectra of the ellipsometric parameters were recorded by a VASE ellipsometer (J.A. Woollam Co.) in the VIS spectral range for incidence angles of 50–80 °. Reflectance measurements were carried out by the same instrument and were numerically treated simultaneously along with the ellipsometry with the help of WVASE commercial software. In the investigated spectral range, the light beam reflected from ZnO nanopillars showed predominantly specular reflection with a negligible diffused component. Ellipsometric spectroscopy, as an indirect characterisation technique, requires a sample model and materials optical constants in the form of table data or parameterised dielectric functions. The sample model consisted of crystalline Si substrate with a SiO_2 native oxide over-layer covered by ZnO nanopillars. These were modelled as a layer with a gradient profile of refractive index. The non-uniform thickness of the ZnO nanorods was also accounted for and was found to be closely related to the recorded depolarisation factor. The optical constants of crystalline Si were taken from the WVASE software database. The ZnO optical constants were parameterised by Cauchy dispersion relation extended with the short-wavelength exponential absorption edge [34]. The upper (surface) part of the ZnO layer, where the implantation of Au ions was expected, was further described by an additional Lorentz harmonic oscillator to account for possible Au local surface plasmon resonance.

3. Results

3.1. Theoretical SRIM simulations of Au-ion interaction with ZnO

For a better understanding of the electronic and nuclear stopping interplay in the implanted and subsequently irradiated ZnO, SRIM calculation [35] of energy stopping was performed.
Additionally, we calculated the projected range using SRIM for the Au-400keV ions as R_P = 65 nm with the standard deviation ΔR_P = 19 nm. SRIM calculation of the Au-ion 400keV depth profiles, O and Zn vacancies creation (displaced energies for Zn and O used in SRIM calculations were referred to in [15,16]) and the energy stopping in ZnO nanopillars has been provided. However, it must be emphasised that SRIM calculation is not capable of taking into account any morphological aspects, so a 500 nm thick ZnO bulk layer is taken into account in the calculation in **Fig. 1a, b**.

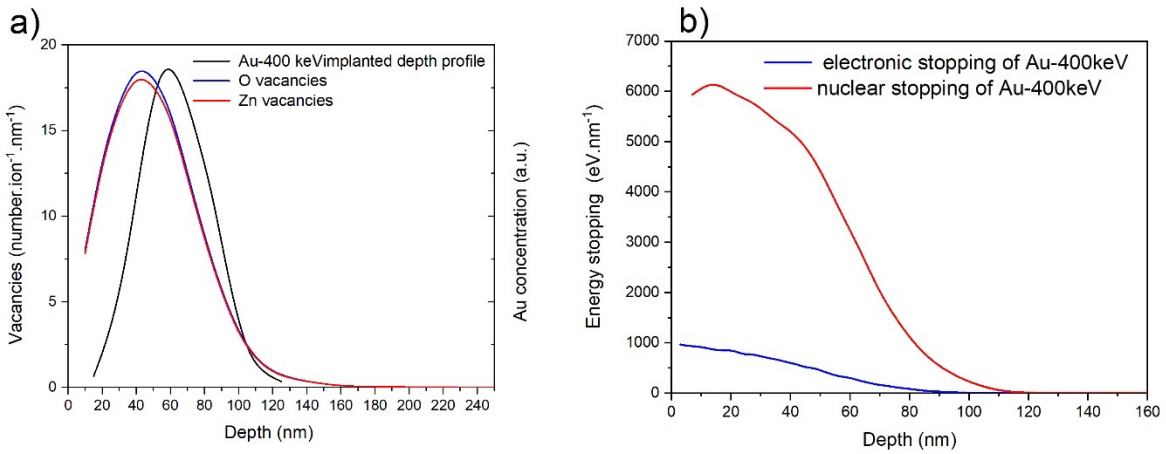

Fig. 1

SRIM calculation of energy stopping of the Au ions used in ZnO nanopillar implantation: Au-400keV energy stopping and O, Zn vacancy depth profiles in a) and b), respectively.

3.2. Elemental and structural analysis by RBS and XRD

The results published recently in [16,32,36] give us a picture of the distinct radiation damage growth, Au-nanoparticle coalescence and optical response in ZnO single crystalline orientations, which should be taken into account in the case of the experiment with ZnO nanopillars implanted by Au-400keV ions. Au nanoparticle coalescence in such ZnO nanopillars and their resulting optical response might differ from ZnO bulk as polar and non-polar facets radiation damage taking place at the same time.

RBS analysis was used to follow, at least qualitatively, the Au distribution in ZnO nanopillars. The pristine ZnO nanopillars were not fully oriented along *c*-axis <0001>, the layer is rather like polycrystalline, so structural analysis based on the ion channelling effect is not possible. Moreover, the depth scale calculation is strongly affected by the complex morphology and high roughness of ZnO nanopillars. Besides, the density cannot be taken as the bulk ZnO density. However, we can qualitatively follow the RBS spectra of ZnO nanopillars deposited on Si, where we saw the modification of the Zn and O signal from the ZnO nanopillars layer. The spectra of the pristine and the as-implanted ZnO nanopillars are presented in **Fig. 2a**. The Au depth profiles are determined and presented in **Fig. 2b**, where we observed a significant shift of the Au concentration maximum towards the depth with the increased Au-ion fluence. In general, the Au depth profiles differ from the SRIM simulation, in that the profiles are broader and exhibited non-normal distribution. Implantation into the nanorods differs from that into compact layers and it suffers from strong straggling of the projected ranges of the implanted ions, so the Au-ions can penetrate much deeper and they cannot be distributed in the defined layer as is predicted by SRIM. However, it can be suggested that the Au coalescence can take a place within the major part of the nanopillars. SRIM calculation of the Au penetration through ZnO has been realised using the ZnO bulk density; thus the observed discrepancy between the SRIM-calculated Au concentration maximum and the experimentally determined Au maximum is understandable in **Fig. 2b**. The annealing slightly influenced the Au depth profiles (see **Fig. 2b**) without a clear correlation with the Au-ion fluence.

ZnO nanopillars exhibited shrinking with the increased Au-ion fluence (see the narrowing of the Zn peak in the RBS spectrum in **Fig. 2a**). This can be connected with the compressive strain in *c*-plane ZnO

(0001) orientation in basal planes, as ZnO nanorods are grown along the *c*-plane, as it stated in our previous works in ZnO implantation with Gd and Au ions in various crystallographic orientations [15, 36]. We did not see significant changes of the Zn peak in the RBS spectra of the annealed samples (not shown); thus, the annealing modifies the internal structure rather than the whole of the nanopillar thickness.

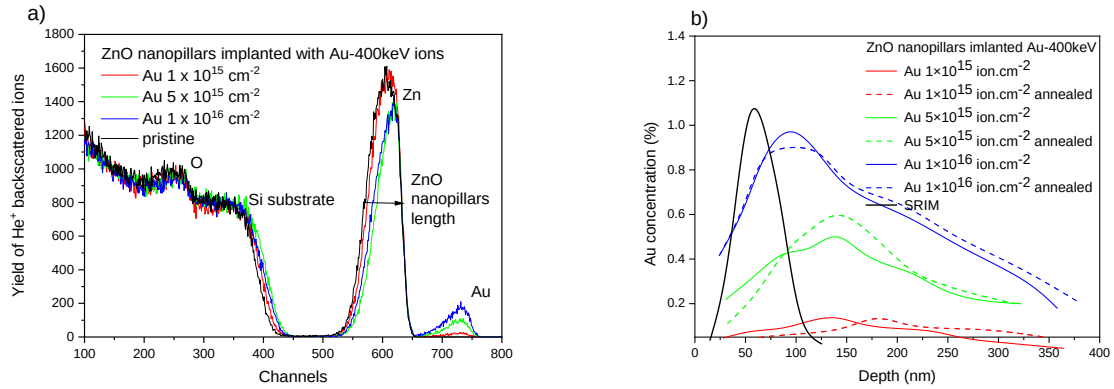

Fig. 2
RBS spectra of the pristine, as-implanted and as-annealed ZnO nanorods implanted with 400 keV Au^+ ions using various fluences in a) and Au concentration depth profiles in Au-implanted ZnO nanorods in b).

XRD analysis of ZnO nanopillars was carried out by combining the MR 2Θ scans with the HR 2Θ/ω scans. The former experiments yielded much higher diffracted intensity, which made it possible to determine the ZnO lattice parameters from a large number of diffraction maxima with sufficient accuracy. Moreover, these measurements are suitable for searching for possible (very weak) diffraction peaks of possible Au nanoparticles. On the other hand, the high diffracted intensity of the 2Θ scans is achieved by a much worse angular resolution, so that these scans cannot be used for the determination of the size of the coherent domains in nanopillars.
Fig. 3 displays the 2Θ scans measured before (blue) and after (red) annealing. All the ZnO diffraction maxima could be identified in the measured curves, while additional non-identified peaks stem most probably from the Si substrate. The peak heights roughly correspond to the calculated intensities; therefore, the ZnO layer is polycrystalline with no strong texture. Au diffraction peaks were not resolved.

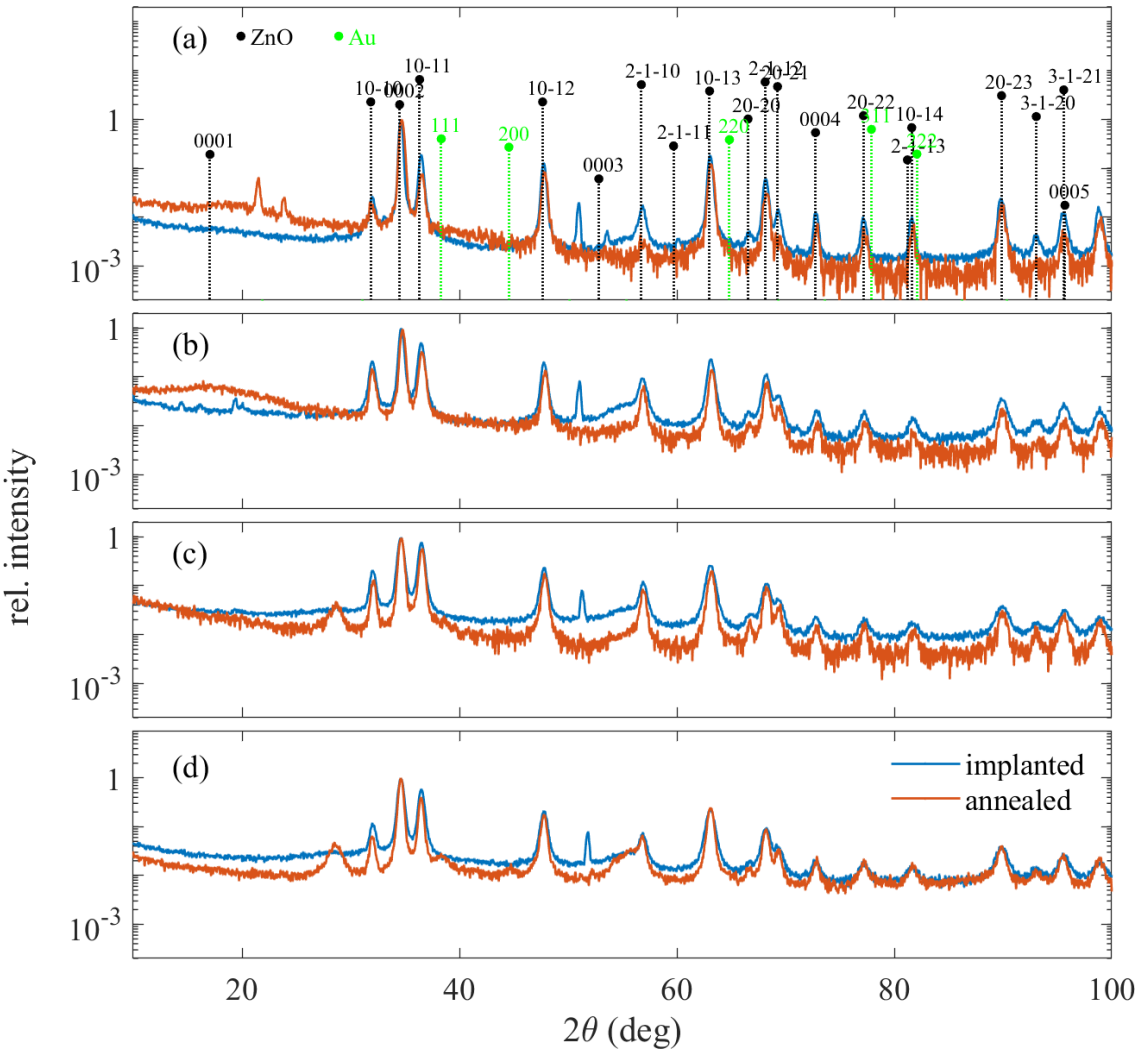

Fig. 3

Medium-resolution 2Θ scans measured before (blue) and after (red) annealing of the pristine sample (a) and samples implanted with fluences of 10^{15}cm^{-2} (b) 5 × 10^{15}cm^{-2} (c) and 10^{16}cm^{-2} (d). In panel (a) we also plotted the theoretical positions and heights of diffraction maxima ZnO (black) and Au (green).

We fitted the individual ZnO diffraction maxima to Voight functions and from the positions of the diffraction maxima we determined the ZnO lattice parameters (see **Table 1**). For this procedure, we used the well-known Cohen–Wagner approach modified for hexagonal crystals [37].

The HR offset scans are displayed in **Fig. 4.** From the integral widths w_j of the HR diffraction maxima, we determined the mean sizes of the coherent domains in the ZnO nanopillars. We assumed that the domains are uniaxial ellipsoids oriented along the [0001], where the mean radii along and across [0001] are denoted R_B and R_V, respectively. We reformulated the Williamson–Hall approach [38] for ellipsoidal domains. The domain radii are determined from the minimum of the following residuum function:

$$S = \sum_j \left[w_j \cos\theta_j - A_j(R_B, R_V) - B \sin\theta_j \right]^2, \qquad (1)$$

where the sum runs over individual diffraction peaks with diffraction angles θ_j, the constant B accounts for a possible microstrain in the nanopillars (assumed isotropic for simplicity), and

$$A_j(R_B, R_V) = \lambda K \frac{\sqrt{R_B^2 + (R_V^2 - R_B^2)\sin^2(\gamma_j)}}{R_B R_V}. \quad (2)$$

Here we denoted $\lambda = 1.5405$ Å as the X-ray wavelength, $K \approx 0.29$ is the shape factor, and γ_j is the angle between the ellipsoid axis (assumed to be parallel to [0001]) and the j-th diffraction vector. The resulting values of $R_{B,V}$ are summarised in **Table 1** as well.

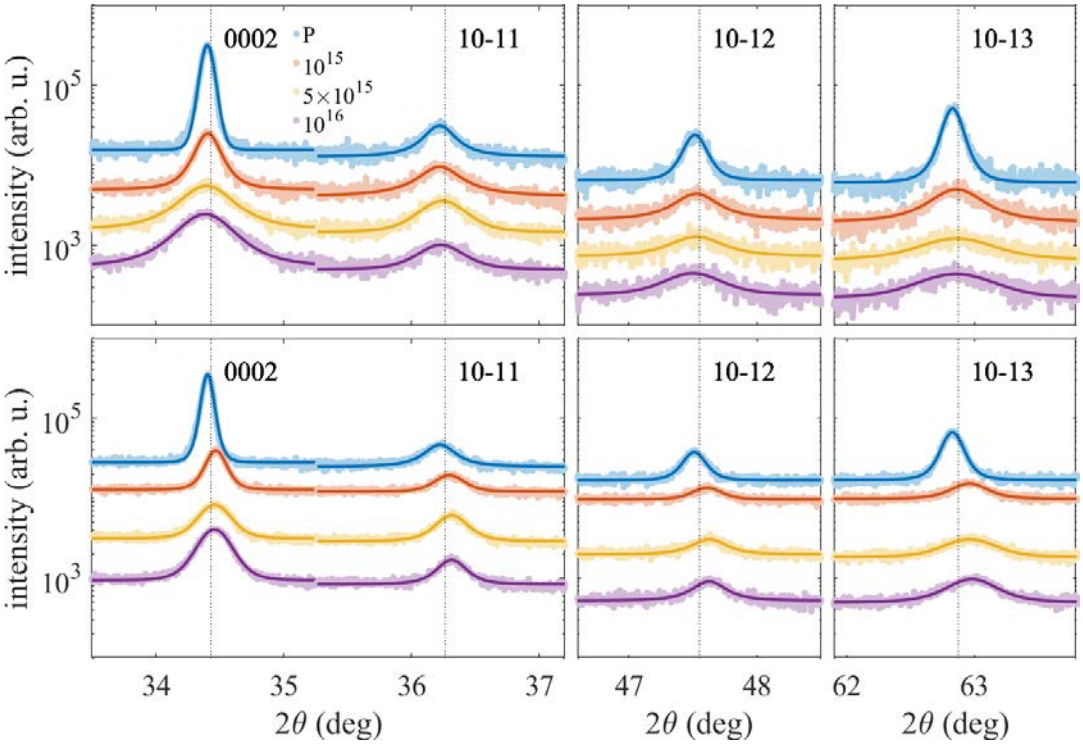

Fig. 4
HR offset scans of several diffraction maxima measured before (upper row) and after (bottom row) annealing and their fit by Voigt functions (lines). The parameters of the curves are the fluences in cm^{-2}, P stands for the pristine sample.

Au-ion fluence (ions. cm^{-2})	ZnO nanopillars – as-implanted; lattice parameters (Å)	ZnO nanopillars – as-annealed; lattice parameters (Å)	ZnO nanopillars – as-implanted; domain radii (nm)	ZnO nanopillars – as-annealed; domain radii (nm)
Pristine	a = 3.244 ± 0.002 *c* = 5.198 ± 0.001	a = 3.242 ± 0.002 c = 5.192 ± 0.001	$R_B = (21 \pm 3)$ $R_V = (59 \pm 1)$	$R_B = (20 \pm 3)$ $R_V = (65 \pm 1)$
1 × 10^{15}	*a* = 3.243 ± 0.002 *c* = 5.192 ± 0.001	a = 3.241 ± 0.002 c = 5.189 ± 0.001	$R_B = (13 \pm 3)$ $R_V = (23 \pm 1)$	$R_B = (18 \pm 3)$ $R_V = (28 \pm 1)$
5 × 10^{15}	a = 3.241 ± 0.002 c = 5.196 ± 0.001	a = 3.243 ± 0.002 c = 5.192 ± 0.001	$R_B = (14 \pm 3)$ $R_V = (11 \pm 1)$	$R_B = (20 \pm 3)$ $R_V = (17 \pm 1)$
1 × 10^{16}	a = 3.243 ± 0.002 c = 5.198 ± 0.001	a = 3.245 ± 0.002 c = 5.194 ± 0.001	$R_B = (15 \pm 3)$ $R_V = (11 \pm 1)$	$R_B = (22 \pm 3)$ $R_V = (17 \pm 1)$

Table 1
The lattice parameters and radii of ellipsoidal coherent domains in ZnO nanorods as implanted with Au-400keV ions and as annealed at the various fluences and compared to the pristine ones.

Table 1 shows that the lattice parameters do not significantly change in the ZnO nanopillars after implantation or annealing. This indicated that Au dopant preferably would not enter any substitutional position, as was already seen in [39], but rather creates Au interstitials and clusters. However, we saw the modification in the basal and vertical domain radii decreasing with increasing Au-400keV ion fluence. After the annealing, we observed the partial restoration of the domain sizes mainly in the basal direction and much less in the vertical direction. However, we can conclude from **Fig. 3** that there is no full restoration of the diffraction peaks, keeping the broader FWHM and the lower intensity compared to the pristine sample. Thus the persisting strained structure is evidenced in the ZnO nanopillars.

3.3. ZnO nanorods morphology (SEM analysis)

Fig. 5 shows the surface morphology and cross-sectional SEM images of the ZnO nanopillars grown on silicon substrates. Medium density and uniformly distributed nanopillars with the upper defined hexagonal facets were grown vertically on the substrates. However, some bending and not perpendicularly oriented nanopillars appeared in the pristine sample (see **Fig. 5a**). The diameters of the nanopillars were analysed from SEM images, being in the broad range from 77–139 nm and the length was deduced from the cross-sectional images, being about 360–400 nm. The morphologies of the nanopillars before and after the Au-400 keV ion implantation are presented with the ascending ion fluence in **Fig. 5 b, c** and **d**, respectively.

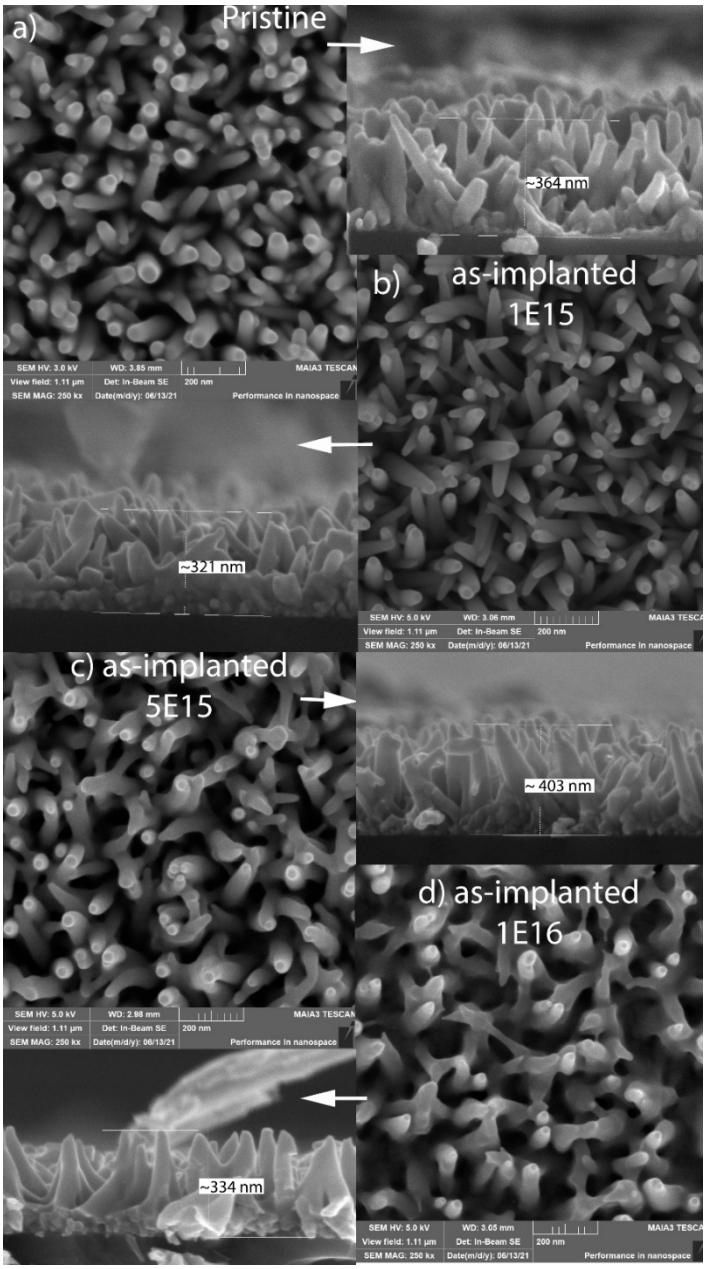

Fig. 5.

SEM analysis of the surface and cross-section morphology of the pristine ZnO nanopillars and as-implanted with the Au-400keV ions at fluences of 1×10^{15}, 5×10^{15} and 1×10^{16} cm^{-2} in a), b), c) and d), respectively.

The compaction and degradation of the ZnO nanopillars can be observed in **Fig. 5** for the higher Au-ion fluences as a result of radiation damage. SEM images of the ZnO nanopillars after the annealing are presented in **Fig. 6** for the higher Au-ion fluences of 5×10^{15} and 1×10^{16} cm^{-2} in **Fig. 6a** and **6b**, respectively. It seems that after the annealing the upper ZnO nanopillar parts are slightly restored, but subsequent compaction of the nanopillar bases appeared.

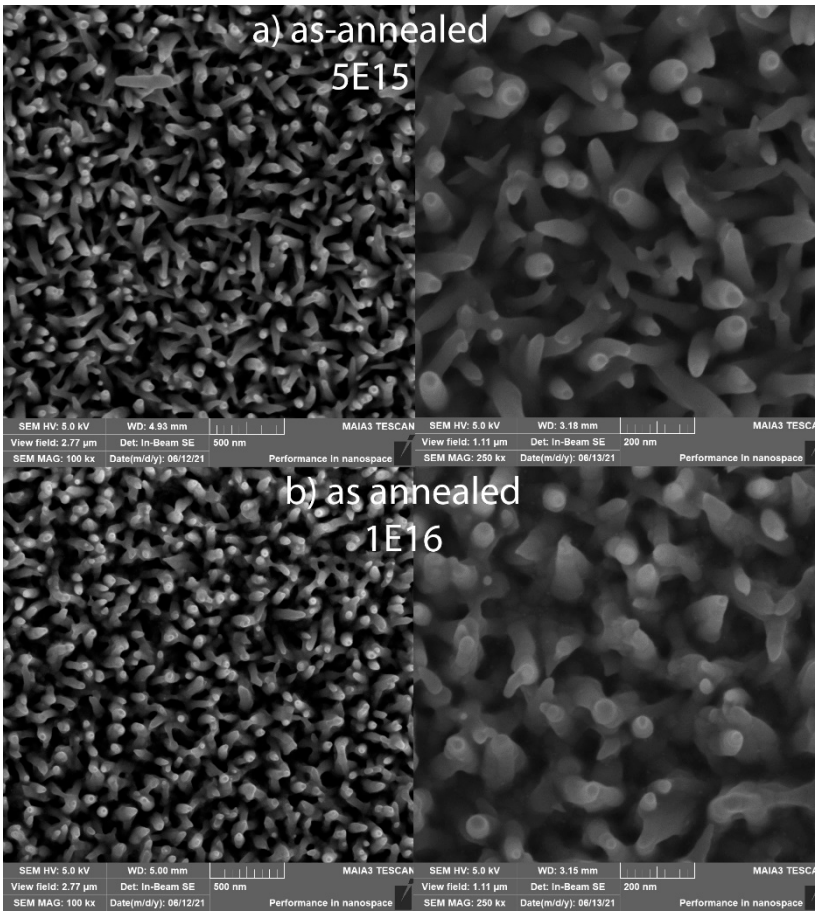

Fig. 6.
SEM analysis of the surface morphology of the ZnO nanopillars as-implanted with the 400 keV Au^+ ions using implantation fluences of (a) 5×10^{15} and (b) 1×10^{16} cm^{-2},annealed at 750 °C for 15 min.

3.4. Optical properties of Au doped ZnO nanorods

We must emphasise that the PL measurement on the ZnO nanopillars implanted with the Au-400keV ions was realised for the as-annealed samples only. The measured PL spectra of the pristine and the as-irradiated and annealed samples are presented in **Fig. 7**. The PL spectra of the pristine samples exhibit the near-band-edge (NBE) luminescence band around 368 nm (assigned to exciton recombination energy 3.37 eV) and the broad deep-level-emission (DLE) band at 650 nm. After the Au-400keV implantation, the intensity of NBE emission decreases. In addition, **Fig. 7a** presents the same data obtained at 10K as raw (unmodified) spectra on a semi-logarithmic scale, revealing the implantation-induced changes of the NBE and DLE intensities as well as of the total PL yield (quantum efficiency). **Fig. 7b** presents PL spectra as a function of the Au implantation fluence plotted on a linear scale, where all curves are normalised with regard to deep-level emission (DLE). This way of presenting the data highlights the implantation-induced spectral changes within the multi-component DLE band. DLE is a decreasing function of the Au-ion fluence, similarly to ion irradiated ZnO nanorods in [40]. The DLE emission consists of several peaks attributed to various defects (V_O - green luminescence, the transition between Zn_i and O_i levels - orange-red etc.) [32].
ZnO nanopillars implanted with Au-400keV ions and annealed exhibited surface plasmon resonance (SPR) activity in the PL spectra measured at 10K in **Fig. 7.** The highlighted SPR peak luminescence is a

growing function of the Au-ion implantation fluence. SPR is evidenced mainly for the highest Au-400keV ion fluence of $1x10^{16}$ cm^{-2} after the annealing and it is centred around 520 nm.

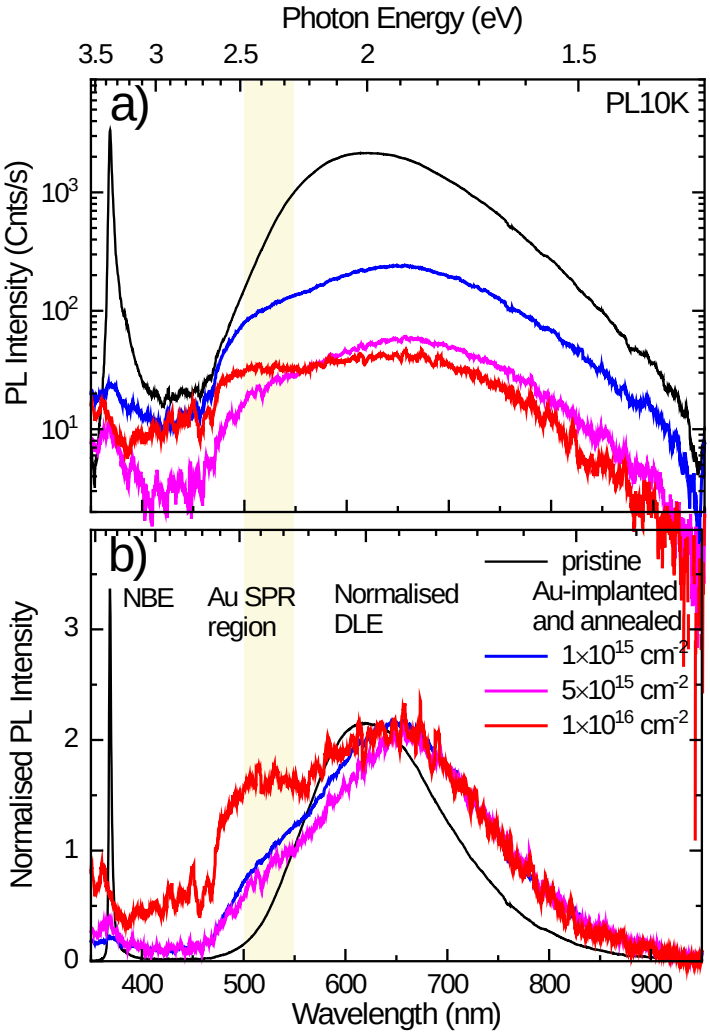

Fig. 7.
PL spectra measured at 10K of the post-annealed ZnO:Au nanopillars implanted at various Au-400keV ion fluences are presented in a) alongside the same data normalised in the DLE region in panel b).

Optical ellipsometry was employed to follow the structural modification in ZnO nanopillars as well as the optical parameters (refraction index and extinction coefficients). It was found that the refraction index in the pristine (**Fig. 8a** – left), as well as in the as-implanted and annealed ZnO nanopillars (**Fig. 8a** – right, **b, c**), exhibited a gradual step-like vertical depth profile. We observed the gradual decrease of the refractive index in the upper part of the ZnO nanopillars from the Si substrate towards the surface of the ZnO nanopillars in pristine samples. The gradual refractive index is seen due to the pre-existing stacking basal faults and as a result of the graded transition introduced by the nanopillar film between the refractive index of air and that of dense ZnO close to the Si substrate (see **Fig. 8a** – left). The Au-ion implantation induced radiation damage. The implanted and post-annealed samples showed the depth profiles of the refractive index, where we observed the decrease of the refractive index in the upper part of the ZnO nanopillars (150–300 nm) and the increase of the bottom part of the nanopillars (0–150 nm). The calculated projected range of the Au-400keV ions is 65 nm. The real

Au depth distribution is even broader than predicted (compared to **Fig. 2b**, the Au distribution was traced by RBS to the depth of about 300 nm. In the upper part of nanopillars with the higher Au concentration, a decreased refractive index was observed, whereas the refractive index in the layer near the Si substrate (about 150 nm) shows values close to the refractive index of bulk ZnO. The thickness of the surface modified layer was modelled for the Au-ion fluences of $1x10^{15}$, $5x10^{15}$ and $1x10^{16}$ cm^{-2} as follows: 160, 107 and 125 nm, respectively. After the annealing there appeared a sharper interface between the nanopillar upper part (150–300 nm) and the compacted bottom part (0–150 nm) see **Fig. 8 a, b, c** – in the right column.

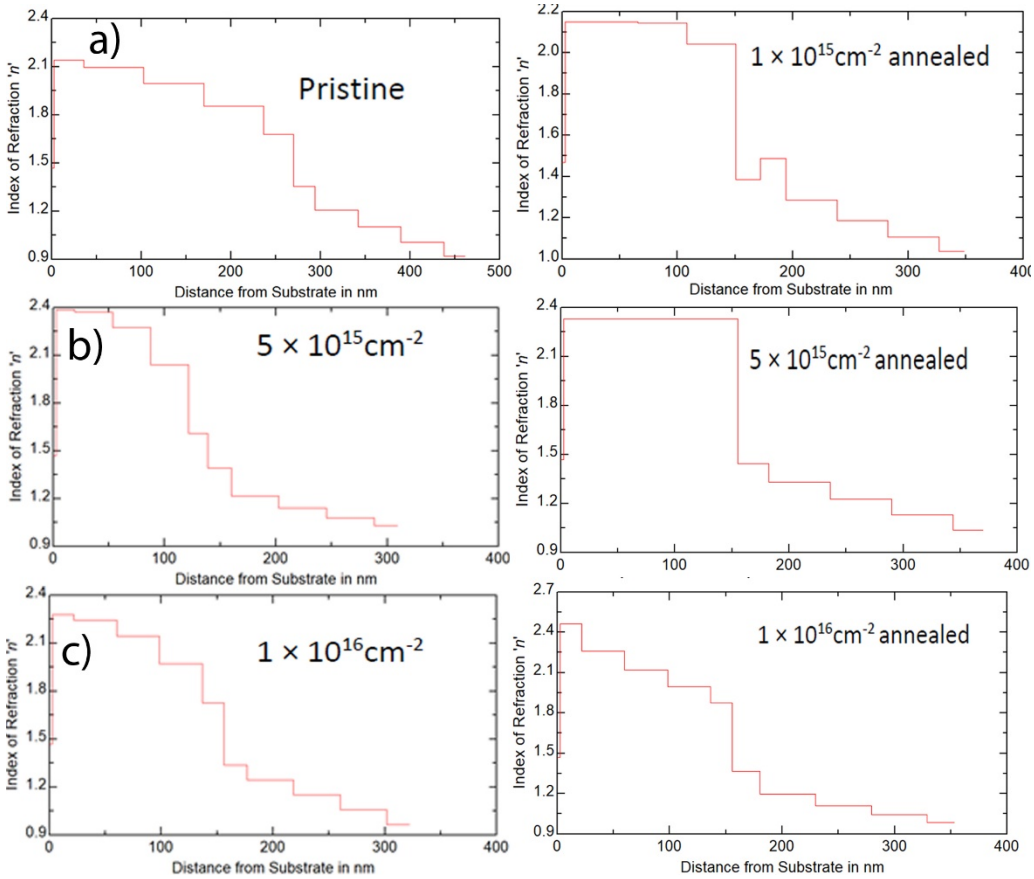

Fig. 8

Optical ellipsometry measured refraction index depth profiles for the ZnO nanopillars. Left panel: the pristine sample in a) the sample implanted with the Au-ions with 5×10^{15} in b) and with 1×10^{16} cm^{-2} in c). Right panel: the sample implanted with the Au-ions with 1×10^{15} cm^{-2} and annealed in a), the sample implanted with the Au-ions with 5×10^{15} and annealed in b) and the sample implanted with the Au-ions with 1×10^{16} cm^{-2} and annealed in c).

The optical activity of Au nanoparticles is presented for the implanted and annealed samples in **Fig. 9**. The absorption maximum ascribed to Au nanoparticles or clusters is evidenced from 500–650 nm. We observe the more pronounced intensity of the absorption peak (SPR) ascribed to the Au nanoparticles with the increased Au-ion fluence. Additionally, the peak maximum is shifting to the depth with the increased fluence (see **Fig. 9**). The annealing caused the absorption peak to shift to the higher

wavelengths and increased the intensity for the lower fluences. For the highest Au-ion implantation fluence of 1×10^{16} cm^{-2}, we do not see this effect.

In the literature [41], the Au nanoparticles decorating ZnO nanowires were analysed by optical spectroscopy. The extinction spectrum contained a distinctive peak at 520 nm which was ascribed to the absorption of visible light by Au nanoparticles with a small degree of agglomeration. However, the Au nanoparticle shape, size, and complexity influenced the absorption maximum being evidenced from 520–600 nm in the literature [14, 42]. We can find the SPR observation in a range of wavelengths of 530∼585 nm in ZnO-Au composites, where the SPR red shift has been ascribed to the agglomeration of Au nanoparticles [43, 44]. The ellipsometric spectra obtained from analysis of pure Au island-like films were fitted using the contributions of the Drude function and Lorentz oscillators in [42], where the SPR positioned around 600 nm has been ascribed to Au nanoparticles 5–15 nm in size. We could suggest from the results that rather non-spherical Au nanoparticles or clusters are present in the ZnO nanopillars.

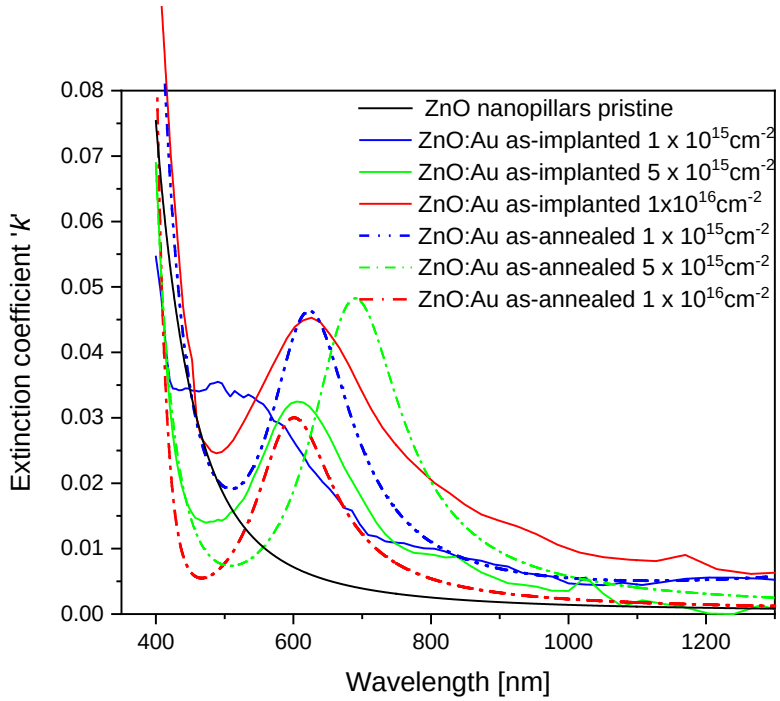

Fig. 9

Optical ellipsometry measurement of extinction coefficients in the as-implanted ZnO nanopillars with the Au-ions at various fluences and subsequently annealed at 750 °C.

4. Discussion

We presented the creation of Au nanoparticles in ZnO nanopillars by ion beam implantation. We followed also the defect accumulation in nanostructured ZnO. For the Au-400keV ions the nuclear stopping dominates and it is much higher than the electronic stopping along most of the ion path. Nuclear collisions will result in the formation of point defects such as vacancies, interstitials, etc. by

displacement of the lattice atoms, which will degrade the crystallinity of the ZnO. The growth rate in the ZnO nanostructures may differ in the polar *c*-plane (0001) compared to the non-polar facets *a*-plane (11-20) and *m*-plane (10-10), where polar ZnO surface growth is not energetically favourable due to the higher surface energy compared to non-polar planes [45]. Thus this effect will play a complex role in the case of ZnO-nanopillars irradiation, where all cuts (crystallographic orientations) are influenced simultaneously. The study in [15, 36] has revealed interesting differences connected to the non-polar facet expansive strain and polar cut compressive strain induced by ions, where spherical point defect formation has been observed, being thermally unstable at 600 °C in polar cut. On the contrary, thermally stable larger extended defects appeared in the non-polar cuts of ZnO. Nanopillars possess a very high effective surface compared to ZnO bulk, which can serve as an effective sink for radiation defects and possible defect annihilation. The energy of impinging ions during ion implantation will be released also in the form of heat and phonons. However, while bulk ZnO has excellent thermal conductivity, nanopillars separated with air can suffer from inefficient heat transfer between them. It was observed in the experiment devoted to Au-1MeV ion irradiation of single crystalline ZnO that the *c*-plane experienced a compressive strain along the *c*-axis and non-polar facets rather than expansive strain [36]. With the increased Au-ion fluence, we observed the narrowing of the ZnO nanopillar upper parts and simultaneously the broadening of the nanopillar base, which could be connected to the compressive strain observed in single crystalline *c*-plane ZnO. Such a shrinking effect was observed also as a consequence of annealing treatment at 900 °C in an oxygen atmosphere in [29], where it was shown that nanowires exhibited rough side facets as the result of annealing.

It was found that implantation-induced effects and thermal effects influence the Au nanoparticle coalescence as well as the quality of the ZnO nanopillars. The implantation at the higher fluences induced the compaction of the nanopillar bases, which are turned into a continuous layer after annealing. We deduced the shrinking of the observed domain sizes in the basal as well as the vertical direction (along the *c*-axis) as a descending function of the Au-ion fluence. This effect is more pronounced for the higher ion fluences and, being evidenced in all the as-annealed samples, such kind of compaction was already shown in the RBS analysis (narrowing of the evidenced ZnO layer thickness) as well as in XRD measurements (decreasing the domain size in the vertical direction).

Thermal degradation seems to affect mainly the ZnO nanopillar shape; however, the internal structure seems to be partially healed up. The radiation damage could be more easily removed due to the defect migration towards the surface, in contrast to the thermal dissipation causing a more distinctive thermal degradation. SEM visualisation of the ZnO nanopillars corroborated the results evidenced by RBS, XRD and ellipsometry. We observed the erosion and narrowing effect of the implanted ZnO nanopillars due to the accumulation of radiation defects and the creation of Au nanoparticles, leading to the compression in the *c*-plane. The dislocation density is suggested to be increased with the decreasing domain sizes evidenced by XRD. These defects seem to migrate into the nanopillar parts closer to the Si substrate. The ZnO nanopillars on the surface include separated regions of air. It seems from SEM and ellipsometric measurement that these air regions between the nanopillars are larger on the top of the nanopillar layer and instead much smaller close to the Si substrate. The heat produced by ions is not efficiently transferred between nanorods in the upper parts; in contrast, this heat transfer will be better in the nanopillar bottom. Under the same irradiation fluence, the temperature of the nanorod arrays will be much higher than that of the bulk ZnO. Such nanopillar upper part

narrowing and nanopillar side-wall modification were recently found in N and H ion irradiated ZnO nanorods in a broad ion fluence range in [27, 28]. This effects are even more pronounced after annealing in connection thermal effects and defect migration at increased temperature. In [43] it was theoretically predicted, and compared to experiments, that the zinc interstitials are mobile species responsible for the healing of the crystal at low temperatures.

The ZnO nanopillar compression was also confirmed with the NBE blue shift to the lower wavelengths (about 361 nm) at the highest Au-ion fluence. Alvi et al. [46] observed a similar blue shift of UV emission in ZnO nanorods/p-GaN light- emitting diodes treated by helium-ion bombardment. The blue shift in the excitonic emission peak can be attributed to the presence of homogeneous compressive strain produced by the Au-ion irradiation increasing the band gap [47]. This effect is in accordance with XRD analysis of the ZnO nanopillars, where the vertical radii of domains are not restored after annealing.

For the single crystalline ZnO, the DLE band appeared around 550 nm - a green emission (GE) - whose origin is assigned to transitions including oxygen-vacancy V_O defects in the ZnO structure [11, 48]. The red centred DLE around 1.8 eV (650 nm) is ascribed to O and Zn vacancies [40]. The DLE red shift observed in the pristine ZnO nanopillars compared to pristine single crystalline ZnO can be connected to the fact that the formation energy of various defects responsible for DLE centred in various wavelengths is also a function of the morphology [40]. As defect formation energies at the surface are lower than in the bulk, they may result in a high defect concentration at the surface. The surface effects become dominant in the photoluminescence, while the surface–volume ratio increases with decreasing nanopillar size. Thus it is clear that the surface effects and surface band bending are important to ZnO-visible PL. The mechanism of how the surface effects influence the photoluminescence is still debatable [40].

SPR activity of the Au nanoparticles was proved by optical ellipsometry as well as photoluminescence in the ZnO nanopillars. Both revealed that clustering of Au particles is highly probable. We did not find evidence of any cubic *fcc* structural form of the Au nanoparticles in bulk ZnO facets in our previous results [36] or in ZnO nanopillars in this experiment. Instead, Au nanoparticles in *hcp* symmetry were found in bulk ZnO, slightly differing in size depending on the ZnO cuts used [36]. In the literature [14, 42] a distinctive peak at 520 nm in extinction spectrum was ascribed to the absorption of visible light by Au nanoparticles with a small degree of agglomeration, instead the complex Au nanoclusters influenced the absorption maximum being evidenced from 520–600 nm [14, 42]. We can find the SPR observation in a range of wavelengths of 530∼585 nm in ZnO-Au composites, where the SPR red shift has been ascribed to the agglomeration of Au nanoparticles or rod-like particles [43, 44]. We could suggest from the results that rather non-spherical Au nanoparticles or clusters are present in the ZnO nanopillars in our case.

5. Conclusions

We presented the capabilities of Au-ion beams with the energy of 400 keV and the fluence above 1×10^{15} cm^{-2} on Au-nanoparticle synthetisation in ZnO nanopillars. We also discussed the difference of Au nanoparticle creation in bulk ZnO based on our previous results as compared to ZnO nanopillars presented in this work, where the creation and optical activation (SPR evidence) of Au nanoparticles seem to be easier to achieve. This could be connected with the fact that ZnO nanopillars exhibited a

polycrystalline character with domains whose boundaries can act as a sink for defects. Au coalescence is supported more than in rigid single crystalline materials. Due to the bending of the nanopillars, both polar and non-polar planes play a role in simultaneous radiation defect commutation, causing modification of the nanopillar shape. We presented results showing that the ZnO nanopillars exhibited a promising ability to create Au nanoparticles with SPR activity. Compared to single crystalline ZnO, the ZnO nanopillars showed effective defect migration and annihilation in nanostructured ZnO due to the large effective surface.

Acknowledgements

The research has been carried out at the CANAM (Centre of Accelerators and Nuclear Analytical Methods) infrastructure LM 2015056. This publication has been supported by OP RDE, MEYS, Czech Republic, under the project CANAM OP, CZ.02.1.01/0.0/0.0/16_013/0001812 and by the Czech Science Foundation (GACR No. 18-03346S).

References

[1] W.J. Weber, D.M. Duffy, L. Thomé, Y. Zhang, The role of electronic energy loss in ion beam modification of materials, Curr. Opin. Solid State Mater. Sci. 19 (2015) 1–11.

[2] G.C. Vásquez, K.M. Johansen, A. Galeckas, L. Vines, B.G. Svensson, Optical signatures of single ion tracks in ZnO, Nanoscale Adv. 2 (2020) 724–733.

[3] J. Lv, X. Li, Defect evolution in ZnO and its effect on radiation tolerance, Phys. Chem. Chem. Phys. 20 (2018) 11882–11887.

[4] Z. Sofer, D. Sedmidubský, S. Huber, J. Hejtmánek, M. Maryško, K. Jurek, M. Mikulics, Flux growth of ZnO crystals doped by transition metals, Journal of Crystal Growth 314 (2011) 123–128.

[5] M. Mikulics, H. Hardtdegen, Nano-LED array fabrication suitable for future single photon lithography, Nanotechnology 26 (2015) 185302.

[6] S. Rehman, R.G. Singh, J.C. Pivin, W. Bari, F. Singh, Structural and spectroscopic modifications of nanocrystalline zinc oxide films induced by swift heavy ions, Vacuum 86 (2011) 87–90.

[7] S. Das, S. Mukhopadhyay, S. Chatterjee, P.S. Devi, G.S. Kumar, Fluorescent ZnO−Au nanocomposite as a probe for elucidating specificity in DNA interaction, ACS Omega 3 (2018) 7494−7507.

[8] V. Gerbreders, M. Krasovska, I. Mihailova, A. Ogurcovs, E. Sledevskis, A. Gerbreders, E. Tamanis, I. Kokina, I. Plaksenkova, ZnO nanostructure-based electrochemical biosensor for Trichinella DNA detection, Sensing and Bio-Sensing Research 23 (2019) 100276.

[9] G. Kumar, L. Tibbitts, J. Newell, B. Panthi, A. Mukhopadhyay, R. M. Rioux, C. J. Pursell, M. Janik, B.D. Chandler, Evaluating differences in the active-site electronics of supported Au nanoparticle catalysts using Hammett and DFT studies. Nat. Chem. 10 (2018) 268–274.

[10] K. Lorenz, E. Wendler, A. Redondo-Cubero, N. Catarino, M.-P. Chauvat, S. Schwaiger, F. Scholz, E. Alves, P. Ruterana, Implantation damage formation in a-, c- and m-plane GaN, Acta Materialia 123 (2017) 177

[11] Y. Azarov, A. Hallén, P. Rauwel, X.L. Du, A.Y. Kuznetsov, and B.G. Svensson, Effect of implanted species on thermal evolution of ion induced defects in ZnO, J. Appl. Phys. 115, (2014) 073512.

[12] M. Ghosh, A.K. Raychaudhuri, Structure and optical properties of Cd-substituted ZnO ($Zn_{1-x}Cd_xO$) nanostructures synthesized by the high-pressure solution route, Nanotechnology 18 (2007) 115618.
[13] J. Zhang, S.Q. Zhao, K. Zhang, J.Q. Zhou, Y.F. Cai, A study of photoluminescence properties and performance improvement of Cd-doped ZnO quantum dots prepared by the sol–gel method, Nanoscale Research Letters 7 (2012) 405.

[14] Y.K. Mishra, S. Mohapatra, R. Singhal, D.K. Avasthi, Au–ZnO: A tunable localized surface plasmonic nanocomposite, Appl. Phys. Lett. 92 (2008) 043107
[15] A. Jagerova, P. Malinsky, R. Miksova, P. Nekvindova, J. Cajzl, S. Akhmadaliev, V. Holy, A. Mackova, Distinct defect appearance in Gd implanted polar and nonpolar ZnO surfaces in connection to ion channelling effect, JVST A 37 (2019) 061406.
[16] A. Jagerova, P. Malinsky, M. Cutroneo, P. Nekvindova, J. Cajzl, A. Michalcova, A. Mackova, Non-polar ZnO facet implanted with Au ions and subsequently modified using energetic O ion irradiation, Nucl. Inst. Meth. B 462 (2020) 16–23.
[17] R. Hauschild, H. Lange, H. Priller, C. Klingshirn, R. Kling, A. Wang, H.J. Fan, M. Zacharias, H. Kalt, Stimulated emission from ZnO nanorods, Phys. Status Solidi B 243 (2006) 853.
[18] M.M.C. Chou, D.R. Hang, C. Chen, S.C. Wang, C.Y. Lee, Nonpolar a-plane ZnO growth and nucleation mechanism on (1 0 0) (La, Sr) (Al, Ta)O3 substrate. Mater. Chem. Phys. 125 (2011) 791.
[19] M.M.C. Chou, D.R. Hang, V. Chen, Y.H. Liao, Epitaxial growth of nonpolar m-plane ZnO (10–10) on large-size LiGaO2 (100) substrates, Thin Solid Films 519 (2010) 3627.
[20] D.R. Hang, S.E. Islam, K.H. Hari Sharma, S.W. Kuo, C.Z. Zhang, J.J. Wang, Annealing effects on the optical and morphological properties of ZnO nanorods on AZO substrate by using aqueous solution method at low temperature, Nanoscale Research Letters 9 (2014) 632.
[21] S. Xu, Z.L. Wang, One-dimensional ZnO nanostructures: solution growth and functional properties, Nano Res. 4 (2011) 1013–98.
[22] E.C. Garnett, M.L. Brongersma, Y. Cui, M.D. McGehee, Nanowire solar cells, Annu. Rev. Mater. Res. 41 (2011) 269–95.
[23] C. Ratajczak, P. Mieszczynski, P. Jozwik, A. Stonert, S. Prucnal, R. Heller, W. Skorupa, J. von Borany, and E. Guziewicz, Ion beam modification of ZnO epilayers: Sequential processing, Phys. Status Solidi A 215 (2018) 1700887.
[24] A. Azarov, B.L. Aarseth, L. Vines, A. Hallén, E. Monakhov, A. Kuznetsov, Defect annealing kinetics in ZnO implanted with Zn substituting elements: Zn interstitials and Li redistribution, J. Appl. Phys. 125 (2019) 075703.
[25] A. Azarov, P. Rauwel, A. Hallén, E. Monakhov, and B.G. Svensson, Extended defects in ZnO: Efficient sinks for point defects, Appl. Phys. Lett. 110 (2017) 022103.
[26] A. Azarov, E. Wendler, E. Monakhov, and B.G. Svensson, Defect stabilization and reverse annealing in ZnO implanted with nitrogen at room and cryogenic temperature, J. Appl. Phys. 123 (2018) 105701.
[27] G. Perillat-Merceroz, F. Donatini, R. Thierry, P-H. Jouneau, P. Ferret, et al. Structural recovery of ion implanted ZnO nanowires. Journal of Applied Physics, American Institute of Physics 111 (8) (2012) 083524.
[28] G. Perillat-Merceroz, P. Gergaud, P. Marotel, S. Brochen, P. Jouneau, and G. Feuillet, Formation and annealing of dislocation loops induced by nitrogen implantation of ZnO, Journal of Applied Physics 109 (2011) 023513.

[29] Jinseok Choi, and Sung Jin An, Effects of arsenic implantation and rapid thermal annealing on ZnO nanorods for *p* type doping, J. Vac. Sci. Technol. B 38 (2020) 052202.
[30] E.N. Epie, D. Scott, W.K. Chu, Manipulating the optical properties of dual implanted Au and Zn nanoparticles in sapphire, Photonics and Nanostructures - Fundamentals and Applications 27 (2017) 17-23.
[31] C. Ronning, P. Gao, Y. Ding, Z. Wang, D. Schwen, Manganese-doped ZnO nanobelts for spintronics, Applied Physics Letters 84 (2004) 783.
[32] J. Cajzl, K. Jeníčková, P. Nekvindová, A. Michalcová, M. Veselý , A. Macková, P. Malinský, A. Jágerová, R. Mikšová, S. Akhmadaliev, Creation of gold nanoparticles in ZnO by ion implantation–DFT and experimental studies, Nanomaterials 10 (2020) 2392.
[33] Y.I. Alivov, Ü. Özgür, S. Dogan, D. Johnstone, V. Avrutin, N. Onojima, C. Liu, J. Xie, Q. Fan, H. Morkoç, Photoresponse of n-ZnO/p-SiC heterojunction diodes grown by plasma-assisted molecular-beam epitaxy. Appl Phys Lett 2005, 86:241108.
[34] J. Mistrik, S. Kasap, H.E. Ruda, C. Koughia, and J. Singh, Optical pProperties of Electronic Materials: Fundamentals and Characterization, in: S. Kasap and P. Capper (Eds.), Springer Handbook of Electronic and Photonic Materials, 2nd ed., Springer International Publishing, Berlin, Heidelberg, 2017, Chap. 3, pp. 47–84.
[35] www.srim.org
[36] A. Mackova, A. Jagerova, P. Malinsky, M. Cutroneo, J. Flaks, P. Nekvindova, A. Michalcova, V. Holy, T. Kosutova, Nanostructures in various Au ion-implanted ZnO facets modified using energetic O ions**,** Physical Chemistry Chemical Physics 22 (41) (2020) 23563–235737.
[37] M.U. Cohen, Precision lattice constants from X-ray powder photographs, Rev. Sci. Instrum. 6 (1935) 68.
[38] T. Ungár, J. Gubicza, G. Ribárik, and A. Borbély, Crystallite size distribution and dislocation structure determined by diffraction profile analysis: principles and practical application to cubic and hexagonal crystals, J. Appl. Cryst. 34 (2001) 298–310.
[39] A . Macková, P. Malinský, A. Jagerová, R. Mikšová, Z. Sofer, K. Klímová, M. Mikulics, R. Böttger, S. Akhmadaliev, J. Oswald, Damage accumulation and implanted Gd and Au position in a- and c-plane, GaN, A, Thin Solid Films 680 (2019) 102–113
[40] T. Wu, A. Wang, L. Zheng, G. Wang, Q. Tu, B. Lv, Z. Liu, Z. Wu, Y. Wang, Evolution of native defects in ZnO nanorods irradiated with hydrogen ion, Scientific Reports 9 (2019) 17393.
[41] W.K. Tana, T. Itob, G. Kawamurab, H. Mutoc, Z. Lockmand, A. Matsuda, Controlled facile fabrication of plasmonic enhanced Au-decorated ZnO nanowire arrays dye-sensitized solar cells, Materials Today Communications 13 (2017) 354–358
[42] S. Wolf, J. Rensberg, A. Johannes, R. Thomae, F. Smit, R. Neveling, M. Moodley, T. Bierschenk, M. Rodriguez, B. Afra, S. B. Hasan, C. Rockstuhl, M. Ridgway, K. Bharuth-Ram, C. Ronning, Shape manipulation of ion irradiated Ag nanoparticles embedded in lithium niobate, Nanotechnology 27 (2016) 145202.
[43] A. Janotti, C. G. Van de Walle, Native point defects in ZnO. Physical Review B 76 (2007) 165202.
[44] R. Viter, Z. Balevicius, A. Abou Chaaya, I. Baleviciute, S. Tumenas, L. Mikoliunaite, A. Ramanavicius, Z. Gertnere, A. Zalesska, V. Vataman, V. Smyntyna, D. Erts, P. Mielee and M. Bechelany, The influence of localized plasmons on the optical properties of Au/ZnO nanostructures, J. Mater. Chem. C 3 (2015) 6815
[45] J. Zúñiga-Pérez, V. Consonni, L. Lymperakis, X. Kong, A. Trampert, S. Fernández-Garrido, O. Brandt, H. Renevier, S. Keller, K. Hestroffer, M.R. Wagner, J.S. Reparaz, F. Akyol, S. Rajan, S.

Rennesson, T. Palacios, G. Feuillet, Polarity in GaN and ZnO: Theory, measurement, growth, and devices, Appl. Phys. Rev. 3 (2016) 041303.
[46] N.U. Alvi, S. Hussain, J. Jensen, O. Nur, M. Willander, Influence of helium-ion bombardment on the optical properties of ZnO nanorods/p-GaN light-emitting diodes, Nanoscale Res Lett. 6 (2011) 628.
[47] A. Galdámez-Martinez, G. Santana, F. Güell, P.R. Martínez-Alanis, A. Dutt, Photoluminescence of ZnO nanowires: A review, Nanomaterials 10 (2020) 857.
[48] A. Jagerová, P. Malinský, R. Mikšová, O. Lalik, M. Cutroneo, O. Romanenko, K. Szökölová, Z. Sofer, P. Slepička, J. Čížek, A. Macková, Modification of structure and surface morphology in various ZnO facets via low fluence gold swift heavy ion irradiation, Surf Interface Anal. 53 (2021) 230–243.